RESEARCH ARTICLE

Key Points:
- CO_2 accumulates at fracture intersections
- CO_2 tends to converge on a single flow path
- Fracture permeability affects CO_2 phase partitioning in flood basalt entablatures

Supporting Information:
- Supporting Information S1
- Data Set S1
- Data Set S2
- Data Set S3
- Data Set S4

Correspondence to:
R. M. Pollyea,
rpollyea@vt.edu

Three-Phase CO₂ Flow in a Basalt Fracture Network

Alec O. Gierzynski[1] and Ryan M. Pollyea[1]

[1]Department of Geosciences, Virginia Polytechnic Institute and State University, Blacksburg, VA, USA

Abstract Geologic CO_2 sequestration in basalt reservoirs is predicated on permanent CO_2 isolation via rapid mineralization reactions. This process is supported by a substantial body of evidence, including laboratory experiments documenting rapid mineralization rates, regional storage estimates indicating large, accessible storage reservoirs, and two successful pilot-scale studies. Nevertheless, there remains significant uncertainty in the behavior of CO_2 flow within basalt fracture networks, particularly in the context estimating physical trapping potential in early time and as CO_2 undergoes phase change. In this study, a Monte Carlo numerical model is designed to simulate a supercritical CO_2 plume infiltrating a low-permeability flood basalt entablature. The fracture network model is based on outcrop-scale LiDAR mapping of Columbia River Basalt, and CO_2 flow is simulated within fifty equally probable realizations of the fracture network. The spatial distribution of fracture permeability for each realization is randomly drawn from a basalt aperture distribution, and ensemble results are analyzed with e-type estimates to compute mean and standard deviation of fluid pressure and CO_2 saturation. Results of this model after 10 years of simulation suggest that (1) CO_2 flow converges on a single dominant flow path, (2) CO_2 accumulates at fracture intersections, and (3) variability in permeability can account for a 1.6 m depth interval within which free CO_2 may change phase from supercritical fluid to subcritical liquid or gas. In the context of CO_2 sequestration in basalt, these results suggest that physical CO_2 trapping may be substantially enhanced as carbonate minerals precipitate within the basalt fracture network.

1. Introduction

As atmospheric CO_2 emissions continue to rise (SIO, 2017), carbon capture and sequestration (CCS) remains an important technology-driven approach for managing anthropogenic CO_2 emissions from fossil fuel powered electricity generation (Pacala & Socolow, 2004). The premise underlying CCS is to capture CO_2 at industrial point sources, and prevent atmospheric release by injecting CO_2 as a pressurized fluid into deep (>750 m) geologic formations. Conventional CCS reservoirs comprise carbonate or siliciclastic formations, including depleted oil and natural gas reservoirs (Benson & Cole, 2008). In conventional CCS reservoirs, short-term ($10^0 - 10^2$ years) CO_2 trapping mechanisms include structural or stratigraphic trapping, residual trapping, and solubility trapping, while permanent mineralization occurs on much longer time scales, e.g., $>10^3$ years (Bachu, 2008). In contrast, basalt reservoirs are presently under investigation for CCS on the basis of rapid mineralization reactions, which result in permanent CO_2 isolation (Bacon et al., 2014; Gysi & Stefánsson, 2011; Matter & Kelemen, 2009; Matter et al., 2016; McGrail et al., 2006, 2017; Schaef et al., 2013).

During CCS in basalt reservoirs, CO_2 dissolution in water results in carbonic acid, which dissociates to provide both the hydrogen ion needed for basalt dissolution and the bicarbonate ion required for carbonate mineral precipitation (Matter & Kelemen, 2009). As basalt dissolves, divalent cations (Ca^{2+}, Mg^{2+}, and Fe^{2+}) are released, which may then react with the available bicarbonate ion to produce carbonate mineral phases, e.g., calcite, magnesite, siderite, and ankerite. This carbonate mineral precipitation releases additional hydrogen ions into solution, which further drives basalt dissolution (Pollyea & Rimstidt, 2017). McGrail et al. (2006) used laboratory experiments on grain-scale Columbia River Basalt Group (CRBG) samples to show that this process occurs on very short time scales, ranging from 10^2 to 10^3 days. In addition, Schaef et al. (2011) performed CO_2-water-basalt reaction experiments with CRBG samples and found increasing reaction rates with increasing temperature and pressure, which suggests that in situ reservoir conditions may be favorable for mineral trapping at field scales.

To further motivate CCS in basalt reservoirs, large igneous provinces occur on all inhabited continents, and basalt comprises the uppermost igneous layer of oceanic crust (Matter & Kelemen, 2009). Goldberg et al.

(2008) estimate accessible offshore storage capacity to be on the order of 250 Gt CO_2 in oceanic basalt off the coast of Washington State, USA, and estimates for the Central Atlantic Magmatic Province hold CO_2 storage potential on comparable scales (Goldberg et al., 2010). In continental flood basalt provinces, CO_2 storage estimates are 36–148 Gt CO_2 in the CRBG, USA and are 150 Gt CO_2 in the Deccan Traps of India (Jayaraman, 2007).

In basalt reservoirs, field experiments have been undertaken at the Wallula Basalt Sequestration Pilot Project in southeastern Washington, USA, (McGrail et al., 2017) and the CarbFix Project at Hellisheidi geothermal power plant in southwest Iceland (Gislason et al., 2010; Matter et al., 2016). These projects were similar in their approach to carbon isolation through CO_2-water-basalt mineralization reactions; however, field implementation in each project differed with respect to the delivery of CO_2. In August 2013, 1,000 t of supercritical CO_2 was injected at the Wallula site (McGrail et al., 2014), and analysis of postinjection sidewall cores showed that carbonate mineral precipitation was widespread in the injection zone (McGrail et al., 2017). Moreover, the carbon isotope values of these carbonate minerals were found to be both distinct from the preinjection samples and correlated with the isotopic signature of the injected CO_2 (McGrail et al., 2017). At the CarbFix field site, CO_2 was coinjected with water, while keeping the CO_2 concentration below its solubility limit in water (Matter et al., 2016). This delivery mechanism was implemented to minimize both degassing potential and buoyancy-driven CO_2 leakage, thus permitting CO_2 injections at moderate depths (400–800 m), where pure CO_2 is subcritical (Sigfusson et al., 2015). To test this injection method, two CO_2 injections were undertaken at the CarbFix site in 2012 (175 and 73 t) and subsequent tracer studies showed that over 95% of the injected CO_2 was isolated within 2 years (Matter et al., 2016).

Although small-scale results from the Wallula and CarbFix site are promising, there remains significant uncertainty with respect to industrial-scale implementation. This uncertainty arises because natural basalt formations are pervasively fractured as a consequence of the steep thermal gradients during cooling and emplacement (Mangan et al., 1986; Zakharova et al., 2012). The fractured nature of basalt reservoirs presents a paradox in which the same fractures that provide storage potential and reactive surface area for mineralization may also provide high-permeability pathways for CO_2 to escape the disposal reservoir (Pollyea & Fairley, 2012a). For example, Pollyea et al. (2014) investigated the basalt fracture paradox for high-rate (21.6 kg s^{-1}) CO_2 injections in basalt reservoirs by combining geostatistical reservoir simulation with kilometer-scale Monte Carlo CO_2 injection modeling to show that spatially correlated and equally probable permeability distributions result in highly variable sealing behavior in east Snake River Plain basalts. Additionally, Jayne and Pollyea (2016) used similar methods to illustrate the wide range of CO_2 plume geometry in flood basalt reservoirs on the basis of kilometer-scale permeability uncertainty in the CRBG. Although these modeling investigations provide valuable constraints on CO_2 migration in response to high-rate CO_2 injections at the reservoir scale, there remains significant uncertainty in the physical trapping potential of basalt entablature zones as buoyancy-driven CO_2 migrates vertically through fracture networks. As a result, this study interrogates supercritical CO_2 infiltrating the fracture network of a CRBG entablature when (1) the spatial distribution of fracture permeability is a priori unknown, and (2) the rising CO_2 passes through the phase change boundary from supercritical fluid to subcritical gas. Results from this study show that (1) CO_2 tends to converge on a single path within the outcrop-scale model domain; (2) CO_2 accumulates at fracture intersections; and (3) CO_2 phase partitioning occurs within a 1.6 m depth interval (thickness) for the modeled scenario.

2. Geologic Setting

The CRBG is a continental flood basalt province comprising a layered assemblage of more than 350 Miocene-age (17.5–6 Ma) basalt flows with an areal extent of approximately 164,000 km^2 in portions of Washington, Idaho, and Oregon, USA (Figure 1a) (Tolan et al., 1989; Vye-Brown et al., 2013). The maximum CRBG thickness is over 4 km near Richland, Washington (Reidel et al., 2013), and total CRBG volume is estimated to be 174,300 $\pm$ 31,000 km^3 (Tolan et al., 1989). The CRBG composition is generally tholeiitic to andesitic basalt with fine-grained texture (Ramos et al., 2005; Reidel et al., 2013). Individual basalt flows are grouped in five primary members, which listed in order of ascending age are: Steens, Imnaha, Grande Ronde, Wanapum, and Saddle Mountains Basalt (Reidel, 2015). The main eruptive phase of the CRBG emplaced the Steens, Imnaha, and Grande Ronde Members, which erupted over the course of 1 million
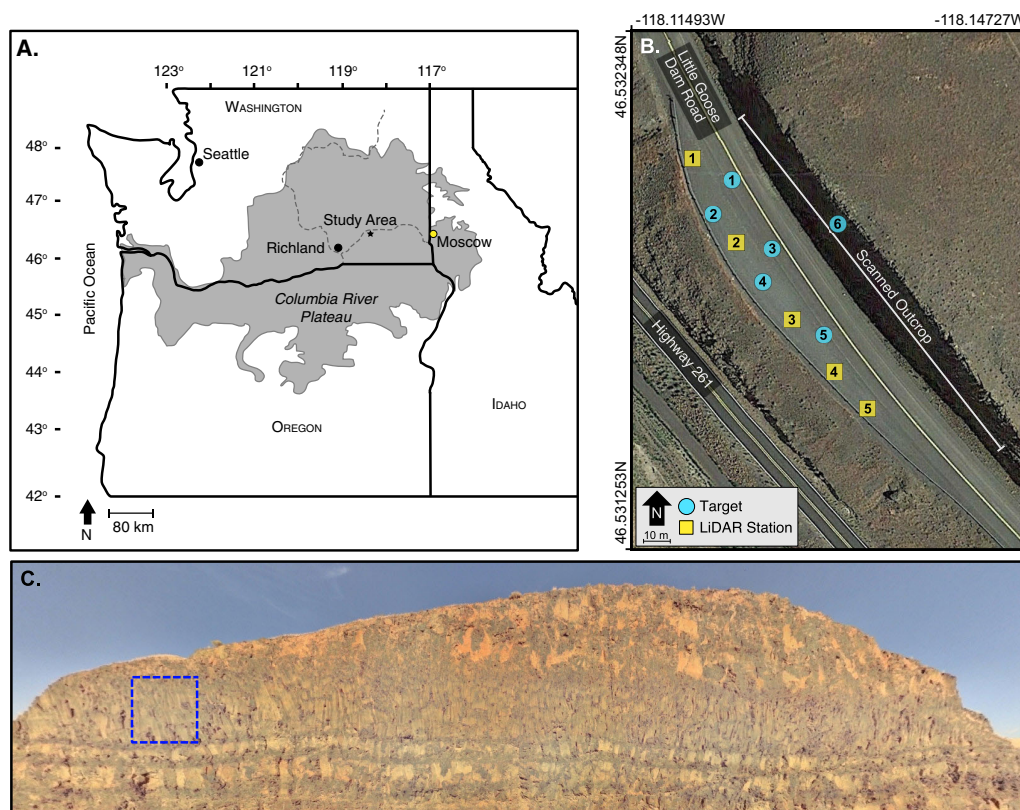
Figure 1. (a) Areal extent of the Columbia River Basalt Group. (b) Study area map and LiDAR station locations at field site. Image from Google Earth[TM]. (c) Image of study area outcrop with dashed blue box corresponding to the fracture network modeled for this study. The blue dashed box is 5 m × 5 m, and the image is not orthorectified.

years, and comprise ∼94% of the CRBG volume (Reidel, 2015). The Grande Ronde is the largest of these members, making up ∼74% of the total CRBG volume (Reidel, 2015) with individual flows often exceeding 1,000 km[3] in volume (Reidel, 2015).

The geologic setting for CRBG eruptions is an area of back arc extension between the Cascades and the Northern Rocky Mountains (Reidel et al., 2013). Volcanism began ∼17.5 Ma when the Yellowstone hotspot was present below the southernmost Steens dike swarm in southern Oregon (Hooper et al., 2002). Over time, the feeder dikes migrated north and the main CRBG eruptive phase occurred from the north-trending Chief Joseph dike swarm, which today is located in southeast Washington and northeast Oregon (Reidel et al., 2013). Northward migration of the feeder dikes is thought to be caused by distortion of the Yellowstone hotspot plume head against the Precambrian margin of North America (Camp, 1995; Reidel et al., 2013). This inference is supported by a coherent isotopic group between the Steens, Imnaha, and Grande Ronde members, suggesting a common magma source (Ramos et al., 2005). Major element and trace element studies show that the plume melted multiple crustal sources, resulting in different bulk properties for individual CRBG members, e.g., individual members include remnants of different crustal lithologies (Ramos et al., 2005). Consequently, individual CRBG members exhibit bulk geochemical homogeneity that has allowed for accurate mapping (Reidel, 2015).

Individual CRBG basalt flows exhibit kilometer-scale lateral dimensions and vertical dimensions ranging from centimeter-scale to greater than 70 m (Mangan et al., 1986). Basalt flow morphology is characterized by: (1) an upper colonnade comprising densely fractured, vesicular flow-tops overlying columnar vertical to subvertical columnar joints, which result from rapid thermal contraction during cooling; (2) a central entablature comprising narrow, fanning columnar joints with hexagonal cross-sectional geometry, which result from thermal interactions between the upper and lower cooling fronts during solidification; (3) lower colonnades with vertical, column bounding joints and, to a lesser extent, horizontal column-normal joints; and (4)
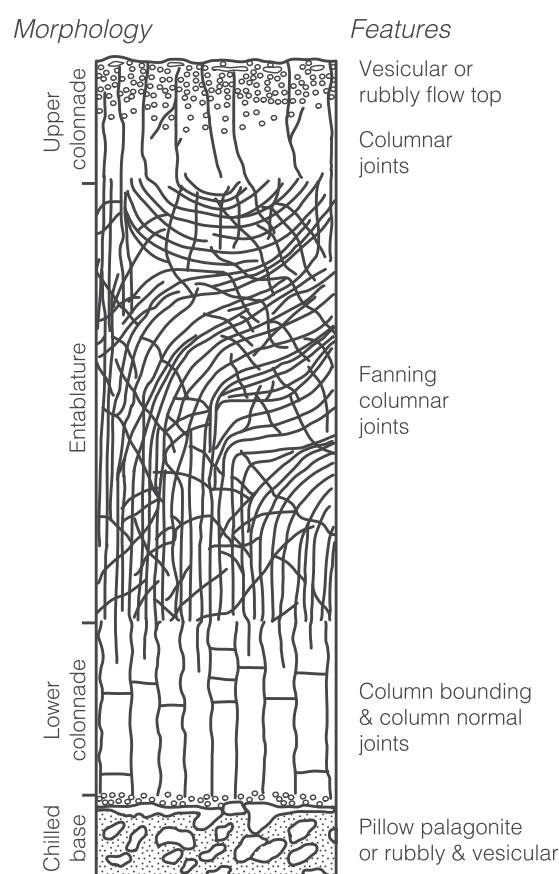
Morphology   *Features*

Figure 2. Generalized schematic of CRBG flow morphology, modified after Mangan et al. (1986).

a chilled base comprising rubbly, vesicular basalt or in some cases pillow palagonite (Figure 2) (Long & Wood, 1986; Mangan et al., 1986). Within CRBG formations, the central entablature is generally considered a barrier to fluid flow on the basis of in situ pumping tests which reveal that hydraulic conductivity within the entablature is approximately 7 orders of magnitude lower than in the densely fracture flow-tops (McGrail et al., 2009). As a result, CCS reservoir configuration in the CRBG comprises the aggregate vertical thickness of an upper colonnade juxtaposed with the lower colonnade of the overlying flow, which is sealed from above by the low-permeability central entablature. This configuration suggests that entablature zones may act as physical traps over a sufficient time frame to accommodate permanent CO_2 isolation through mineralization (McGrail et al., 2006). This study is designed to assess how permeability uncertainty in the fracture network of a CRBG entablature affects physical trapping potential as CO_2 enters from an underlying reservoir.

3. Methods

This study utilizes multiphase, multicomponent numerical modeling to investigate the influence of fracture permeability on CO_2 infiltration and phase change(s) within a basalt entablature fracture network. The model scenario is designed to represent supercritical CO_2 entering a basalt entablature from below when the pressure-temperature conditions are near the phase change boundary for CO_2. As a result, this study provides first-order estimates of buoyancy-driven leakage potential as CO_2 density decreases during phase changes from supercritical fluid to subcritical liquid or gas. For this study, free CO_2 can be in any of three phases, which are (1) supercritical fluid, (2) subcritical liquid, and (3) subcritical gas; however, the supercritical phase fluid and subcritical gas are the predominant fluid phases in the modeling results. The model domain comprises a 5 m × 5 m fracture network developed using outcrop-scale data acquired by ground-based light-detection and ranging (LiDAR) (sections 3.1 and 3.2). To account for the uncertainty associated with fracture permeability at depths of interest (>750 m) for CO_2 sequestration, a synthetic fracture permeability distribution is produced on the basis of core-scale fracture aperture measurements from the literature (section 3.3). This fracture permeability distribution is implemented for a Monte Carlo numerical model comprising 50 equally probable, 2-D realizations of the same fracture network. In order to isolate the effects of permeability uncertainty, the fracture network geometry is identical for each realization; however, the spatial distribution of fracture permeability is randomly drawn from the synthetic permeability distribution. Three-phase relative permeability and capillary pressure effects are accounted for using generic characteristic curves (section 3.4). Vertical CO_2 flow is simulated in each fracture network model (section 3.5), and e-type estimates are computed for fluid pressure and CO_2 saturation over the complete ensemble of 50 equally probable fracture permeability distributions (section 3.6). The bulk fluid and rock properties are listed in Table 1.

3.1. LiDAR Acquisition

Ground-based LiDAR scans were acquired from a basalt outcrop near Starbuck, Washington, in November 2015 (Figure 1b). The selected outcrop was approximately 100 m wide by 10–15 m tall (Figure 1c). Terrestrial LiDAR scans were acquired with a Z + F Imager 5010x, which is a phase-based laser scanner with a range of 187 m and range

Table 1
Model Parameters

Parameter	Value	Units
$T_\circ$	32	°C
TDS	270	mg L^{-1}
c_P	840	J kg^{-1} °C^{-1}
κ_T	2.11	W m^{-1} °C^{-1}
ρ_r	2,950	kg m^{-3}
ϕ_f	0.1	–
ϕ_m	0.01	–
S_{ar}	0.63	–
S_{lr}	0.01	–
S_{gr}	0.001	–
n	1.4	–
α_{gl}	10.8	–
α_{la}	6.0	–

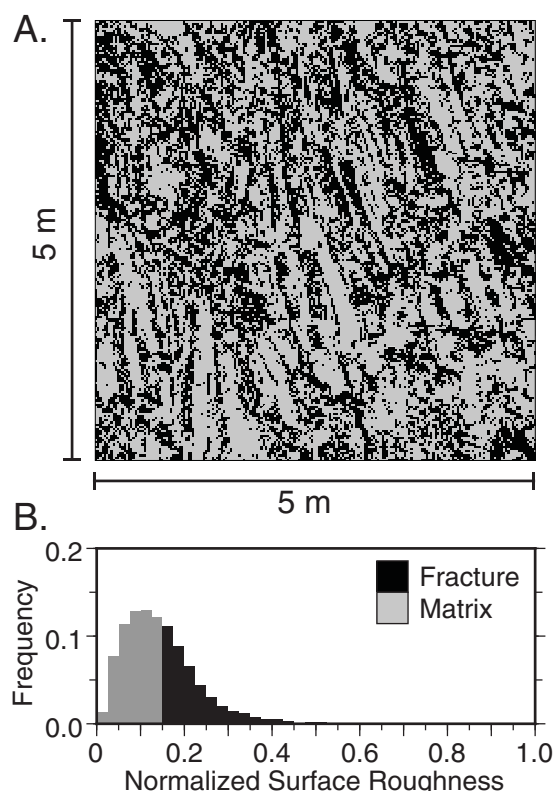*Note.* See Notation section for description of symbols.

Figure 3. (a) LiDAR-based 2-D fracture network map developed for this study. The fracture network is modeled with 0.025 m grid resolution from a 5 m × 5 m section of a Columbia River Basalt flow entablature (Figure 1c, blue dashed box). The fracture model comprises 40,000 grid cells. Matrix and fracture cells are denoted by gray and black shading, respectively. (b) Probability distribution of normalized surface roughness for the fracture network in Figure 2a. Shading denotes the proportion of the probability distribution assigned to matrix cells (gray) and fracture cells (black).

noise of ~0.4 mm at 25 m. LiDAR data were acquired at five scanning stations selected along the outcrop, and each scan was specified to overlap the previous scan by ~25% (Figure 1b). In order to facilitate accurate point cloud registration, six Z + F Profi targets were deployed in a staggered geometric configuration along the outcrop and each scan acquired a minimum of four targets. The LiDAR stations and target locations were geospatially referenced with a Trimble Geo7x hand held GPS configured for subcentimeter resolution. The outcrop LiDAR scans were merged using Z + F Laser Control software with mean registration error of 1.7 mm, standard deviation of 1 mm, and maximum deviation of 5.6 mm. Following registration, errant data points (e.g., reflections from dust, insects, and occasional traffic) were filtered from the combined data set manually, and the postprocessed outcrop point cloud data was exported in ASCII format.

3.2. Fracture Network Model

The fracture network developed for this study comprises a 5 m × 5 m subsection of the postprocessed point cloud (Figure 1c). This subsection of the outcrop is located entirely within the entablature portion of the basalt flow. The entablature is of particular interest here because it has been proposed as the confining unit for CO_2 trapping on the basis of effective permeability values of $\sim 10^{-18}$ m^2 (McGrail et al., 2009). In order to extract the entablature fracture distribution from the subsampled region, the raw point cloud is processed using the surface roughness algorithm developed by Pollyea and Fairley (2011, 2012b). In this method, the point cloud is discretized into a regular Cartesian grid and an orthogonal regression plane is fit to the points within each grid cell. The surface roughness of each grid cell is then calculated as the standard deviation of point-to-plane distances. This method returns surface roughness values on a ratio scale for each grid cell, and (Pollyea & Fairley, 2011) showed that 2-D fracture network models can be extracted by implementing a binary transform to normalized surface roughness data. The premise underlying this binary transform is that surface roughness is larger for grid cells intersecting fracture edges and/or prominences in the outcrop, and, as a result, this information is exploited to assign each grid cell to either "fracture" or "matrix" subdomains. Consequently, unique hydrogeological properties can be assigned within each subdomain for numerical flow modeling.

For this study, surface roughness is calculated within the 5 m × 5 m entablature subsection over a regular Cartesian grid discretized with 0.025 m (2.5 cm) resolution. This results in a 2-D model domain comprising 200 grid cells along each axis (40,000 total grid cells). After normalizing surface roughness to range between 0 and 1, the binary threshold delineating fracture and matrix grid cells is determined by trial-and-error to be the lowest value for which the resulting fracture network is visually realistic and at least two fractures are continuously connected through the domain (Figure 3).

3.3. Fracture and Matrix Permeability

Basalt matrix permeability is uniformly specified as 10^{-20} m^2 on the basis literature values ranging between 10^{-17} and 10^{-24} m^2 for basalt matrix permeability (Bertels et al., 2001; Nara et al., 2011; Walker et al., 2013a, 2013b). In contrast, the fracture permeability for 0.025 m grid resolution is unknowable at depths of interest (>750 m) for CO_2 sequestration; however, Lamur et al. (2017) report core-scale basalt fracture permeability of $\sim 10^{-15}$ m^2 at effective stresses up to 30 MPa. As a result, this study implements a Monte Carlo numerical model comprising 50 individual simulations within the same fracture network. In this approach, the spatial distribution of fracture permeability in each model domain is randomly selected from a synthetic lognormal fracture permeability distribution.

The synthetic fracture permeability distribution is based on Lindberg (1989), which reports spatially uncorrelated and lognormally distributed fracture aperture (b) measurements from 3,194 CRBG joints. This aperture distribution is described by mean aperture of 2.66×10^{-4} m and standard deviation of 4.89×10^{-4} m. For this study, the fracture aperture distribution is converted to a fracture permeability (k_f) distribution on the basis of the parallel-plate cubic law ($k_f = b^2/12$) (Ge, 1997; Witherspoon et al., 1980), which is assumed valid on the basis of the 0.025 m grid discretization. Application of the cubic law to the Lindberg (1989) aperture distribution results in a mean fracture permeability of 5.9×10^{-9} m^2 with corresponding standard deviation of 1.99×10^{-8} m^2. Lindberg (1989) also shows that CRBG fracture apertures are spatially uncorrelated, and, as a result, the fracture permeability distribution developed here is reproduced in 50 equally probable realizations of the same fracture map, while the spatial distribution within each realization is spatially uncorrelated.

Because the Lindberg (1989) distribution was measured from ex situ core samples, each simulated fracture permeability distribution is scaled to account for the effects of loading at depths of interest of CO$_2$ sequestration. In doing so, the simulated permeability value assigned to each grid cell is scaled by subtracting a mean fracture permeability that is assumed to be representative of in situ conditions. For this study, the in situ mean fracture permeability is estimated using the weighted geometric mean for the case when (1) effective (bulk) permeability is constrained by field-scale pumping tests and (2) matrix permeability is reasonably approximated by core-scale experimental data. In the context of effective medium theory, the general form of weighted geometric mean permeability is given by:

$$k_{eff} = \exp\left(\frac{\sum_{i=1}^{N} \omega_i \ln k_i}{\sum_{i=1}^{N} \omega_i}\right) \qquad (1)$$

where, k_{eff} is effective permeability, k_i is the permeability of subdomain i, and ω_i is a weighting function (Fairley, 2016; Rubin, 2003). For the bimodal fracture network model, equation (1) is expanded and rearranged to solve for mean fracture permeability:

$$k_f = \exp\left(\frac{\ln k_{eff} - \omega_m \ln k_m}{\omega_f}\right) \qquad (2)$$

where, subscripts f and m refer to the fracture and matrix subdomains, respectively. For this study, k_{eff} is specified as 10^{-18} m^2, which is a typical value for pumping tests in CRBG entablatures (McGrail et al., 2009; Wood & Fernandez, 1988); k_m is equal to the 10^{-20} m^2 (discussed above); and the weighting function is based on the probability distribution of each subdomain, so that ω_m and ω_f are 0.58 and 0.42, respectively, (Figure 3b). Equation (2) results in a mean in situ fracture permeability of 5.78×10^{-16} m^2, which is comparable to permeability tests in artificially induced basalt cores at effective stresses comparable to depths of interest for CO$_2$ storage (Lamur et al., 2017). The difference between this in situ mean k_f and the Lindberg (1989) mean permeability is subtracted from each simulated fracture permeability in the ensemble of 50 equally probable realizations, which effectively translates the Lindberg (1989) distribution to depths of interest for CO$_2$ sequestration while maintaining the same degree of variability about the mean. The resulting fracture permeability distribution for one equally probable realization is illustrated in Figure 4a with the corresponding permeability histogram shown in in Figure 4b.

3.4. Three-Phase Constitutive Relations

For this modeling study, characteristic curves are used to simulate the effects of relative permeability and capillary pressure as functions of aqueous phase saturation. Relative permeability and capillary pressure for multiphase CO$_2$ and water systems have not yet been finalized (Gran et al., 2017). Consequently, the three-phase relative permeability model developed by Stone (1970) is implemented with constraints based on multiphase experiments between N$_2$ and water in a basalt fracture (Bertels et al., 2001). For this study, fitting relative permeability curves with data from multiphase N$_2$-water experiments is justified on the basis of Pini and Benson (2013), which shows very small differences in relative permeability characteristics between gN$_2$-water, gCO$_2$-water, and scCO$_2$-water fluid pairs at pressure and temperature conditions relevant for CCS (Pini & Benson, 2013). After fitting relative permeability curves, the resulting parameters are then used for the three-phase capillary pressure model developed by Parker et al. (1987). The relative permeability and capillary pressure models used for this study are shown graphically in Figure 5 with parameters in Table 1, and a detailed discussion of each model follows.
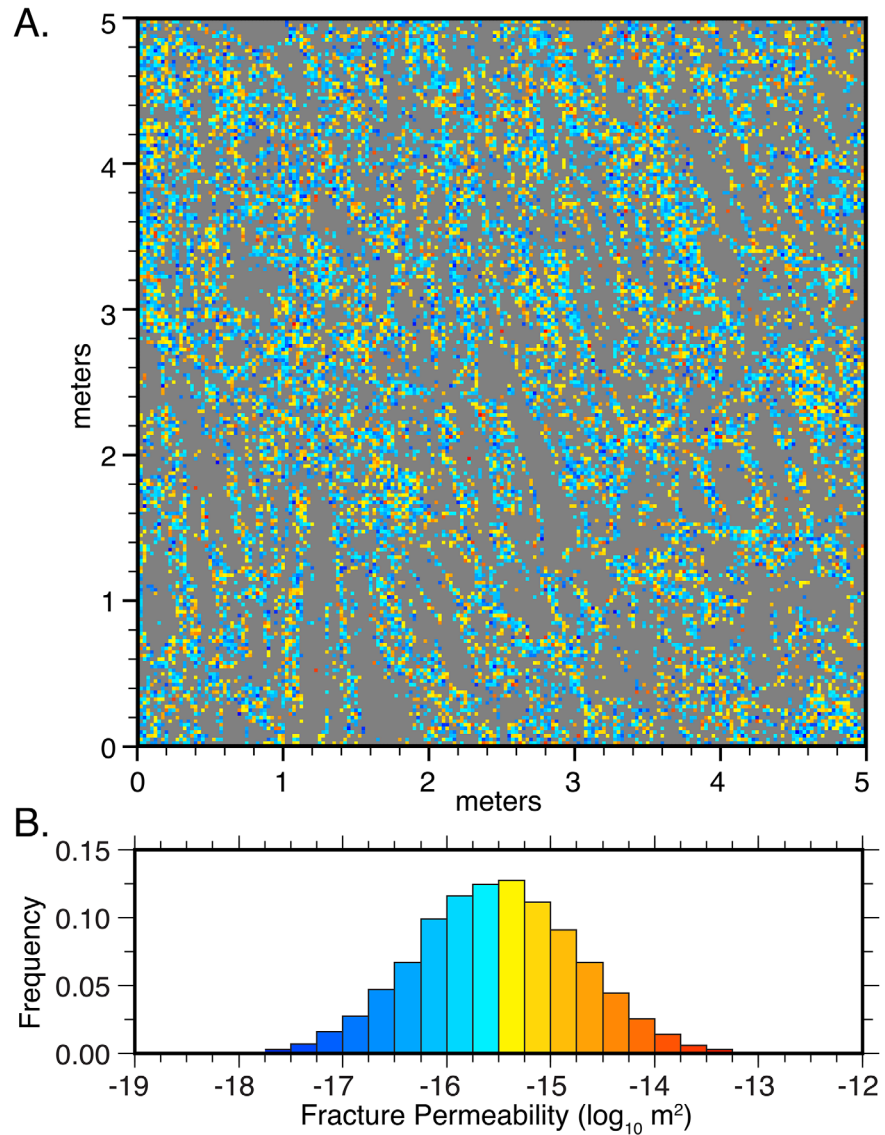
A.

B.

Figure 4. (a) One equally probable fracture permeability distribution developed by scaling the Lindberg (1989) aperture distribution to depths of interest for CO_2 sequestration. Gray shading denotes matrix permeability ($\log_{10} k_m = -20$) and color range denotes fracture permeability ($\log_{10} k_f$). (b) Histogram of $\log_{10} k_f$ for the simulated permeability distribution in Figure 4a. Color bars correspond with scale for $\log_{10} k_f$ in Figure 6a.

3.4.1. Relative Permeability

To account for the effects of multiple fluid phases in each grid cell, the relative permeability model originally proposed by Stone (1970) is implemented for each fluid phase as:

$$k_{rg} = \left(\frac{S_g - S_{gr}}{1 - S_{ar}} \right)^n \tag{3}$$

$$k_{ra} = \left(\frac{S_a - S_{ar}}{1 - S_{ar}} \right)^n \tag{4}$$

$$k_{rl} = \left(\frac{1 - S_g - S_a - S_{lr}}{1 - S_g - S_{ar} - S_{lr}} \right) \left(\frac{1 - S_{ar} - S_{lr}}{1 - S_a - S_{lr}} \right) \left(\frac{(1 - S_g - S_{ar} - S_{lr})(1 - S_a)}{1 - S_{ar}} \right)^n \tag{5}$$

where, k_{rg}, k_{ra}, and k_{rl} represent relative permeability for the nonwetting gaseous or supercritical (nonwetting) CO_2 phase, aqueous (wetting) phase, and nonwetting liquid CO_2 phase, respectively; S_g and S_a are
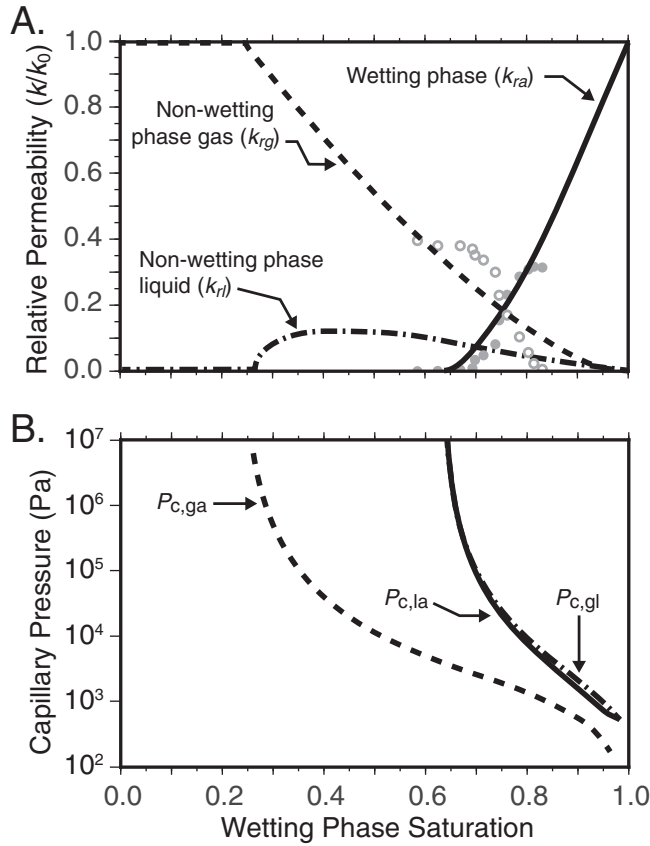
gaseous (or supercritical) and aqueous phase saturation, respectively; S_{gr}, S_{ar}, and S_{lr} are irreducible saturation parameters for the gaseous (or supercritical) CO_2 phase, aqueous phase, and nonwetting liquid CO_2 phase, respectively; and n is a phase interference parameter. The Stone (1970) relative permeability model is based on channel theory, which states that in any given channel, only one fluid is active. Furthermore, this relative permeability model assumes that the wetting phase tends to remain in small pore spaces, while the nonwetting phases preferentially occupy larger pores. Because of this phase separation, interactions of the liquid nonwetting phase with water and gas are considered separate events (Stone, 1970). To implement this model within the basalt fracture network, equations (3) and (4) are fit to data from two-phase (k_{rg} and k_{ra}, respectively) relative permeability experiments reported by Bertels et al. (2001) for water and nitrogen in a basalt fracture (Figure 5a and Table 1). At the time of this writing, relative permeability for the nonwetting liquid CO_2 phase (k_{rl}) has not been measured experimentally.

3.4.2. Capillary Pressure
Capillary pressure effects are modeled using the three-phase model reported by Parker et al. (1987). In this formulation, the capillary pressure across each fluid interface is calculated with the following set of equations:

$$P_{c,gl} = -\frac{\rho_a g}{\alpha_{gl}} \left[\bar{S}_l^{-1/m} - 1 \right]^{1/n} \tag{6}$$

$$P_{c,ga} = -\frac{\rho_a g}{\alpha_{la}} \left[\bar{S}_a^{-1/m} - 1 \right]^{1/n} - \frac{\rho_a g}{\alpha_{gl}} \left[\bar{S}_l^{-1/m} - 1 \right]^{1/n} \tag{7}$$

$$P_{c,la} = P_{c,ga} - P_{c,gl} \tag{8}$$

where, $P_{c,gl}$ is capillary pressure across the interface between gaseous (or supercritical) and liquid phases, $P_{c,ga}$ is capillary pressure across the interface between gaseous (or supercritical) and aqueous phases, and $P_{c,la}$ is capillary pressure across the interface separating the nonwetting phase liquid and aqueous phases. In addition, g is acceleration due to gravity, ρ_a is aqueous phase density, m is the Van Genuchten (1980) phase interference parameter ($m = 1 - 1/n$), and α_{la} and α_{gl} are strength parameters for the liquid-aqueous and gaseous-liquid interfaces, respectively. In this formulation, capillary pressure calculated as a function of effective saturation ($\bar{S}$), where $\bar{S}_a$ is effective aqueous phase saturation ($\bar{S}_a = (S_a - S_{ar})/(1 - S_{ar})$) and $\bar{S}_l$ is effective nonwetting phase liquid saturation ($\bar{S}_l = (S_g + S_l - S_{ar})/(1 - S_{ar})$). Equations (6–8) are parameterized using the α parameters presented by Parker et al. (1987) and irreducible wetting and nonwetting phase saturation values found by fitting the relative permeability model to Bertels et al. (2001) experimental data (Figure 5b and Table 1).

3.5. Numerical CO_2 Flow Simulation
The numerical model simulates a scenario in which free-phase, supercritical CO_2 has accumulated below a basalt flow entablature at depths approaching CO_2 phase change boundary. The code selection for this study is TOUGH3 (Jung et al., 2016), which solves energy and mass conservation equations for nonisothermal, multiphase flows in porous geologic media. Here TOUGH3 is compiled with fluid property module ECO2M, which simulates mixtures of water, CO_2, and NaCl, as well as CO_2 phase change between liquid, gaseous, and supercritical state (Pruess, 2011). In this formulation, CO_2 phase partitioning in each grid cell is modeled on the basis of equilibrium thermodynamics for the temperature range $12^{\circ} \leq T \leq 110^{\circ}$ and fluid pressure up to 60 MPa (Pruess, 2011).

Initial conditions are specified with a hydrostatic pressure gradient ranging from 7.35 to 7.39 MPa, which corresponds with a saturated depth of $\sim 750-755$ m. The initial temperature field is specified as 32°C, and thermal effects are accounted for in the simulations. These initial conditions are consistent with field
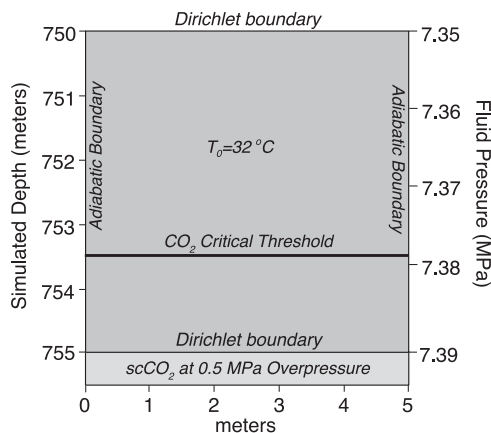
Figure 5. (a) Labeled curves represent the three-phase relative permeability model of Stone (1970). Curves are fit to Bertels et al. (2001) experimental data for water-nitrogen relative permeability in a basalt fracture: solid and open circles are wetting and nonwetting phase relative permeability, respectively. (b) Three-phase capillary pressure model by Parker et al. (1987). See Notation section for a description of the symbols.

Figure 6. Schematic illustration of the initial and boundary conditions implemented for each CO_2 model in this study.

conditions encountered at the Wallula Basalt Sequestration Pilot Project in southeast Washington State, USA (McGrail et al., 2009). Furthermore, this initial condition is designed such that free-phase supercritical CO_2 will encounter the critical point within the model domain, and thus undergo phase change to subcritical liquid or gas. Adiabatic pressure and temperature conditions are specified on the lateral model boundaries. Fluid is allowed to leave the model domain by specifying a Dirichlet condition at the upper boundary, and temperature is held constant at 32°C at the upper and lower boundaries. The basal boundary simulates an accumulation of supercritical CO_2 below the basalt flow entablature by specifying a Dirichlet condition as fully saturated with CO_2 at 0.5 MPa overpressure and 32°C (Figure 6). Hydraulic and thermal properties are listed in Table 1.

In order to quantify the effects of fracture permeability uncertainty within the model domain, 50 individual CO_2 flow models are performed within the synthetic fracture network. The decision to simulate 50 equally probable reservoirs represents a balance between computational efficiency and simulating sufficient data to capture a wide range of possible outcomes. For each numerical model, the fracture network geometry and initial and boundary conditions are identical; however, the permeability for each fracture cell is randomly drawn from the synthetic permeability distribution developed in section 3.3 (Figure 4b).

In closing this description of model development and specification, a brief mention about model limitations is warranted. Specifically, this modeling study does not account for geochemical processes responsible for basalt dissolution and carbonate precipitation, which are likely to affect fracture permeability. For example, Luhmann et al. (2017a, 2017b) show that CO_2-spiked water flowing in a basalt fracture results in minor permeability reduction due to mineral precipitation at low flow rates, while higher flow rates result in order-of-magnitude permeability enhancement due to rapid dissolution and transport. Similarly, Adeoye et al. (2017) indicate that the temporal evolution of fracture geometry under net dissolution is strongly influenced by mineral grain size. Although these processes will likely impose dynamically changing permeability in a natural fracture network, such scaling laws remain beyond the current state-of-the-art. Consequently, the numerical model developed here is relevant primarily in early time prior to widespread mineralization ($< \sim 10$ years).

3.6. Data Analysis

The ensemble of 50 simulations is analyzed using e-type estimates, which yield the mean and variance of a simulated variable within each grid cell of the domain (Deutsch & Journel, 1998). For example, the mean value of simulated fluid pressure ($\bar{P}_{f(x,z)}$) in each grid cell of the Monte Carlo model is computed for the ensemble of 50 simulations as,

$$\bar{P}_{f(x,z)} = \frac{1}{50} \sum_{i=1}^{50} P_{f,i(x,z)} \tag{9}$$

where, $P_{f,i(x,z)}$ is the simulated fluid pressure at location (x, z) for simulation i. The corresponding measure of uncertainty around the mean at each grid cell is computed as the standard deviation ($\sigma_{Pf(x,z)}$),

$$\sigma_{Pf(x,z)} = \sqrt{\frac{1}{50} \sum_{i=1}^{50} \left(P_{f,i(x,z)} - \bar{P}_{f,(x,z)} \right)^2} \tag{10}$$

In addition to e-type estimates for fluid pressure, equations (9) and (10) are implemented for wetting and nonwetting phase saturations to assess variability in phase partitioning as a function of permeability uncertainty.

4. Results and Discussion

Each numerical model accounts for 10 years of simulation time with data output at 1, 5, and 10 years. The results of two individual simulations are illustrated in Figure 7, which shows total free-phase CO_2 saturation
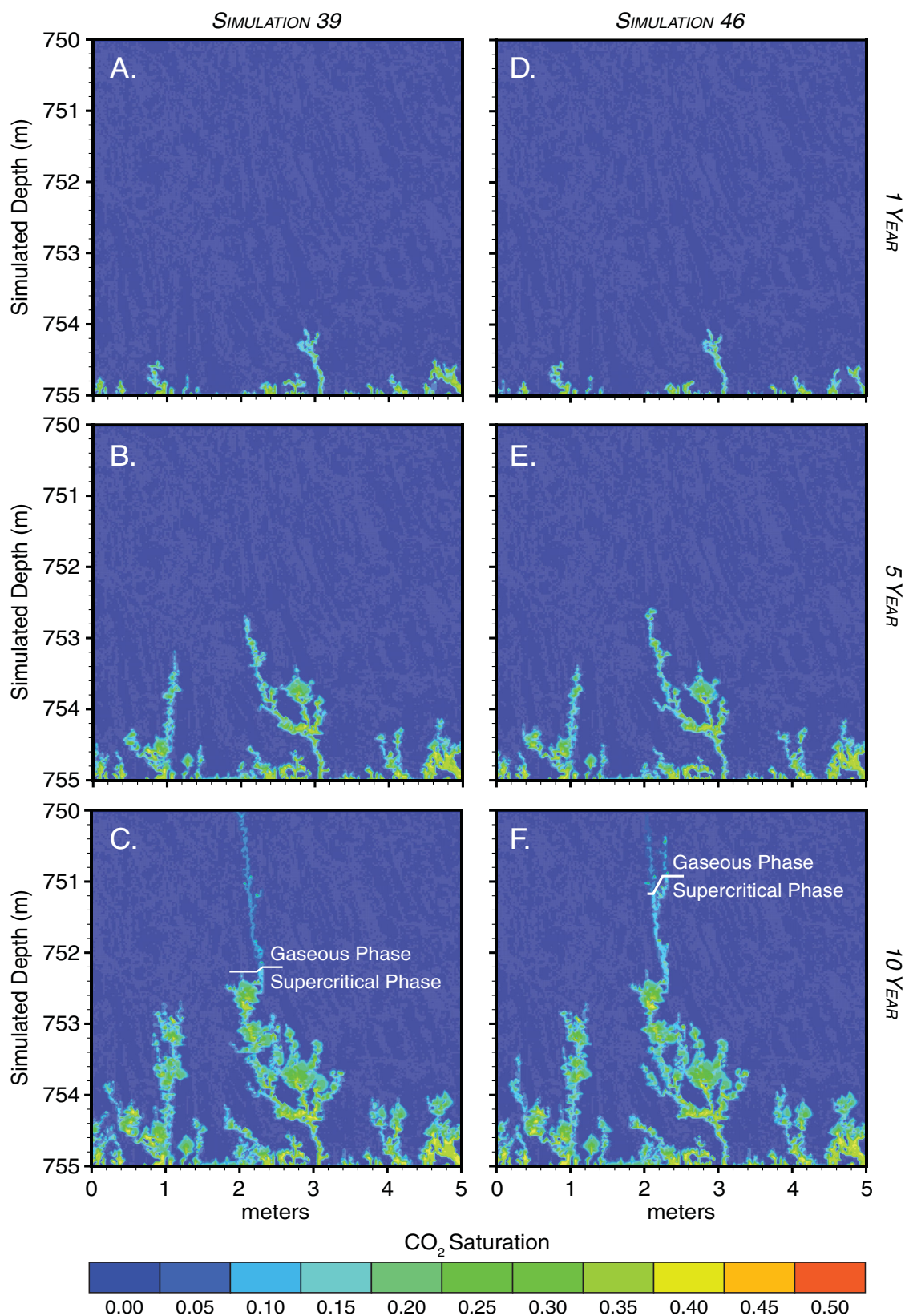
Figure 7. Temporal evolution of total CO_2 saturation for end-member simulations: simulation 39 at (a) 1, (b) 5, and (c) 10 years; simulation 46 at (d) 1, (e) 5, and (f) 10 years.

at 1, 5, and 10 years of simulation time. These individual simulations are labeled 39 and 46, and represent the minimum and maximum extent of CO_2 infiltration for the complete ensemble, i.e., these simulations are end-members of the model behavior after 10 years. The e-type estimates (equations (9) and (10)) resulting from the complete ensemble at 1, 5, and 10 years are shown for total free-phase CO_2 saturation in Figure 8, and the corresponding e-type estimates for fluid pressure are shown in Figure 9. Phase partitioning between supercritical- and gas-phase CO_2 after 10 years of simulation is illustrated in Figure 10.

4.1. One Year

After 1 year of simulation, all free CO_2 remains in the supercritical phase for the end-member simulations, 39 and 46 (Figure 7). In both simulations, CO_2 rises ~1 m into the fracture network, and follows the same pathways with comparable saturation levels. The fluid pressure distribution in simulations 39 and 46 (not shown) propagates upward through the domain according to fracture network geometry. Consequently, fluid pressure decreases nonlinearly with elevated pressure occurring below blockages in the fracture pathways, and lower pressures along clear conduits.

E-type results for total CO_2 saturation and fluid pressure after 1 year are presented in Figures 8 and 9, respectively. The ensemble mean supercritical CO_2 saturation is comparable to the results for simulations 39 and 46, with mean CO_2 saturation ranging between 0.10 and 0.36 in the conductive fractures. The variability of this ensemble behavior is relatively low, as indicated by the corresponding standard deviation of ~0.06 to 0.10, which is governed by variability in the permeability distribution. Nevertheless, the largest degree of CO_2 saturation variability occurs in conductive fractures, particularly where a single flow path diverges into two or more flow paths. The ensemble mean fluid pressure after 1 year of simulation indicates the pressure perturbation induced by infiltrating CO_2 is maximized in conductive fractures as pore space is drained (Figure 9a). Interestingly, fluid pressure variability is also maximized in the conductive fractures, where the maximum deviation is ~72 kPa (Figure 9c). This effect is most pronounced at the leading edge of the advancing CO_2, where aqueous phase relative permeability in basalt fractures decreases substantially at low CO_2 saturation levels (Bertels et al., 2001). This result agrees with Pollyea (2016), which shows that fluid pressure accumulation in basalt reservoirs is governed primarily by drainage of the aqueous phase. Similarly, the gradient in fluid pressure variability is highest below constrictions or blockages in the main fracture pathways, which can occur when a conductive fracture terminates or as a result of comparatively low fracture permeability. In contrast, fluid pressure variability within conductive fracture is smallest at locations where CO_2 initially enters the fracture network. The ensemble model results after 1 year indicate that CO_2 flow paths and fluid pressure distribution are controlled primarily by fracture network geometry, while variability in CO_2 saturation is governed by interactions between fracture permeability and network geometry.

4.2. Five Years

After 5 years, the end-member simulations 39 and 46 show little discernible difference in both CO_2 saturation (Figures 7b and 7e) and fluid pressure distribution (not shown). As with the 1 year end-member simulations, all free CO_2 remains in the supercritical phase as the fluid pressure diffusion from the lower boundary pushes the critical point of CO_2 to more shallow depths. E-type results for total CO_2 saturation and fluid pressure are shown in Figures 8b, 8e, 9b, and 9e, respectively. These results indicate the presence of three conductive fractures, within which supercritical CO_2 has migrated ~2 m from the basal boundary. Mean CO_2 saturation is ~0.2 in the conductive fractures, although substantially higher CO_2 saturation levels occur in disconnected fractures as CO_2 accumulates. In addition, elevated CO_2 saturation occurs at fracture junctions, where a single conductive fracture splits into two or more flow paths. This suggests that intersecting fractures may focus the effects of mineralization, as elevated free CO_2 maintains an equilibrium supply of hydrogen and bicarbonate ion to drive both basalt dissolution and carbonate precipitation (Pollyea & Rimstidt, 2017). Interestingly, the standard deviation of CO_2 saturation is generally highest along continuous sections of the fracture network, suggesting that fracture permeability strongly influences CO_2 saturation within the conductive portion of the fracture network (Figure 8e).

The mean fluid pressure distribution after 5 years of simulation is generally similar to the 1 year results (Figure 9b); however, the corresponding variability is substantially lower across most of the domain (Figure 9e). This suggests that flow paths for CO_2 imbibition and aqueous phase drainage stabilize within the fracture network. Nevertheless, a sharp discontinuity in mean fluid pressure emerges at the horizontal position ~2 m from the origin and 752.6 m simulated depth (Figure 9b). This discontinuity is collocated with a small
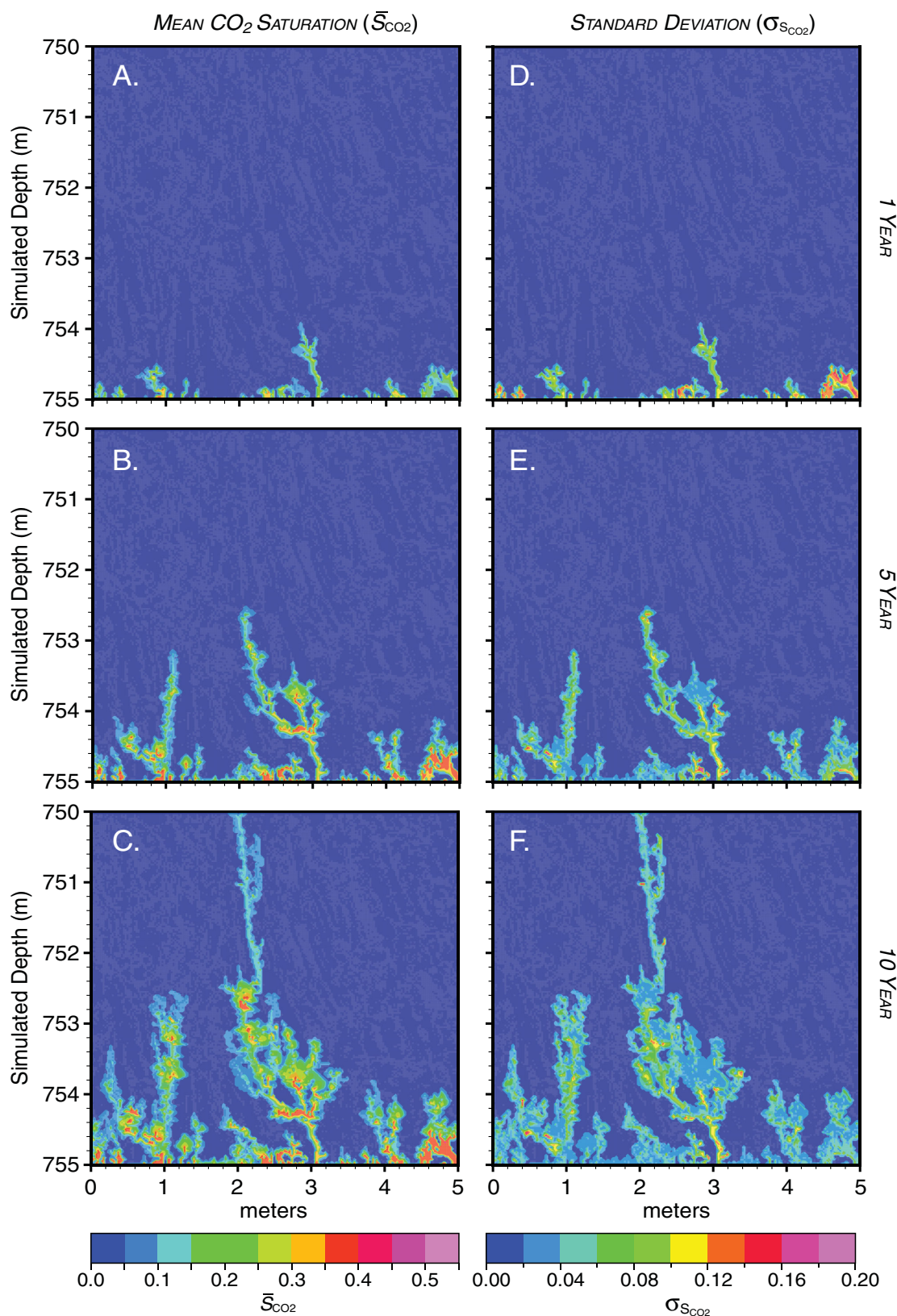
Figure 8. Ensemble results (e-type) of total CO_2 saturation for the Monte Carlo model (N=50 simulations). Results are calculated with equations (9) and (10) for total CO_2 saturation. Mean CO_2 saturation at (a) 1, (b) 5, and (c) 10 years, and (d–f) corresponding standard deviation for each mean.
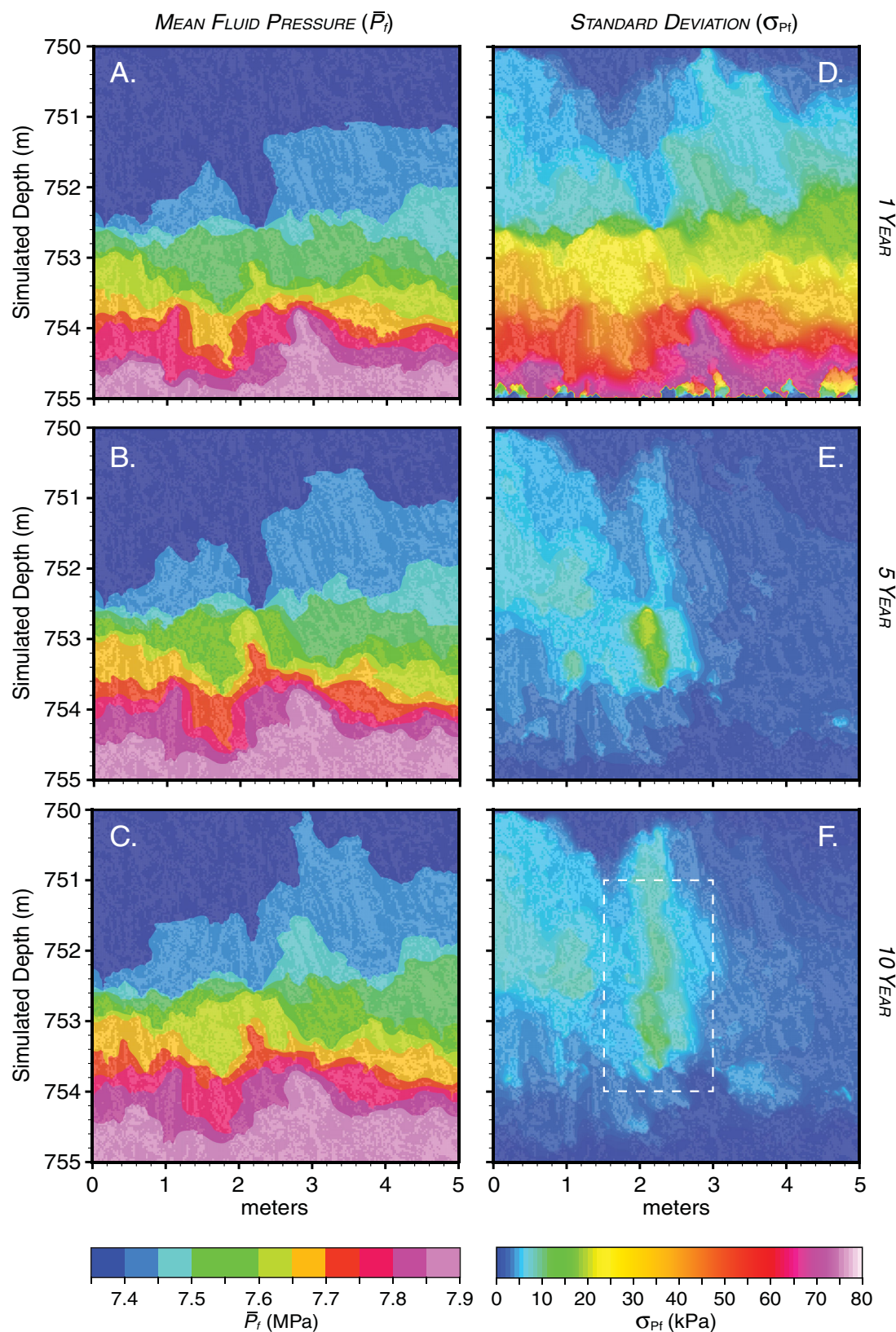
Figure 9. Ensemble results (e-type) of fluid pressure for the Monte Carlo model (N=50 simulations). Results are calculated with equations (9) and (10). Mean fluid pressure at (a) 1, (b) 5, and (c) 10 years, respectively, and (d–f) the corresponding standard deviation for each mean. Dashed box in Figure 9f is presented in Figure 11.
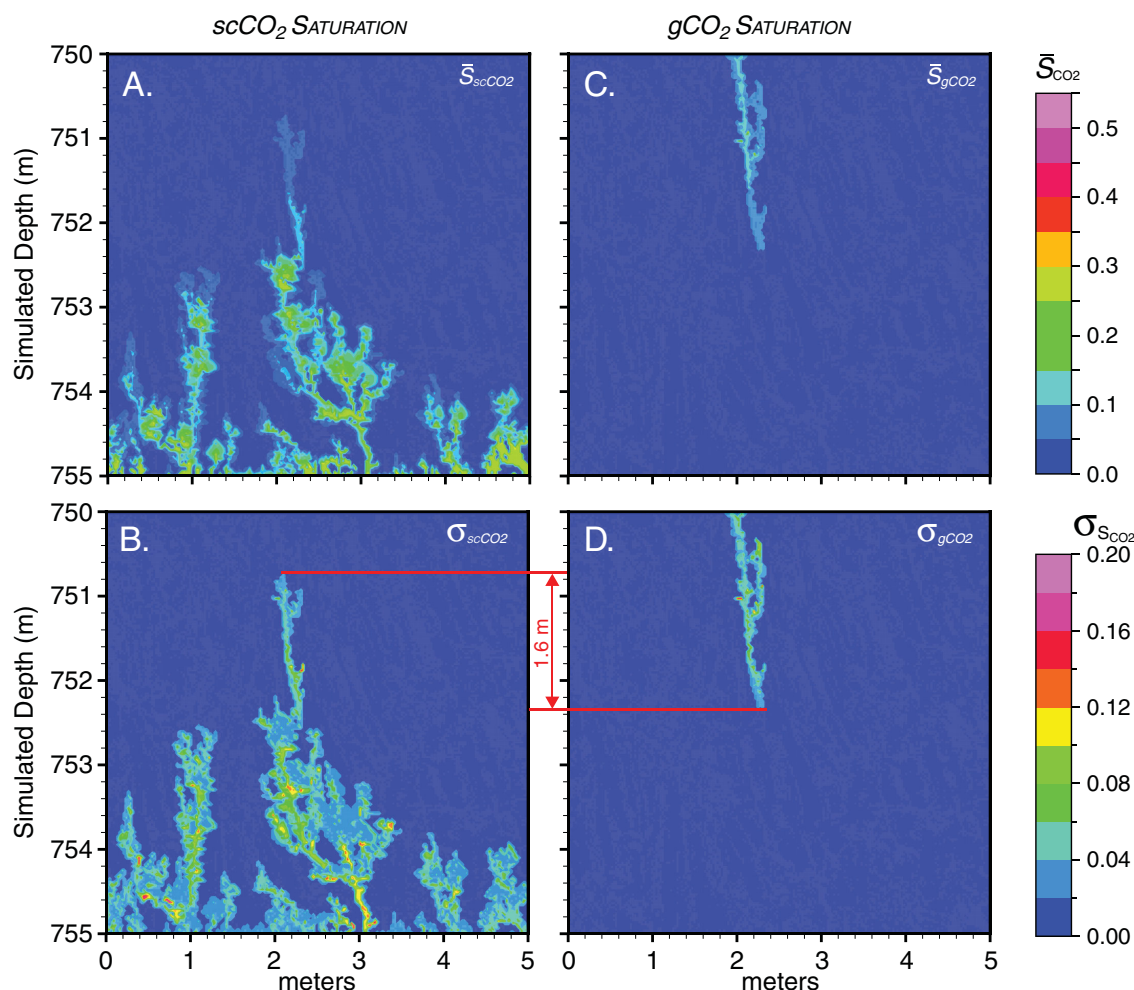
Figure 10. Ensemble results (e-type) of (a, b) supercritical phase CO_2 and (c, d) subcritical gas phase CO_2 for the Monte Carlo model (N=50 simulations) after 10 years of simulation. The depth-interval for which fracture permeability governs phase partitioning is shown as red lines in Figures 10c and 10d.

region of elevated uncertainty, which is a constriction in the conductive fracture, where the flow paths bends to the right and permeability within a single grid cell is the dominant control on flow through the network. The region above this constriction is marked by a near-vertical channel of moderate fluid pressure uncertainty. Although this channel comprises no CO_2 at the 5 year time step, the fluid pressure variability suggests that drainage is underway, thus foreshadowing the development of a primary flow path within the fracture network. Although similar behavior is seen in the fluid pressure distribution at horizontal positions less than 2 m from the origin, the effects are much more diffuse as the conductive fractures in this region terminate into the basalt matrix.

4.3. Ten Years

After 10 years, the end-member simulations 39 and 46 comprise three-phase CO_2 conditions with supercritical fluid and subcritical gas as the predominant phases (Figures 7c and 7f). The notable difference between the end-member simulations is illustrated by (1) the depth of phase change and (2) the flow path taken by gas phase CO_2 at shallow depths in the domain. In simulation 39, phase change occurs at ~752.2 m simulated depth; however, the depth of phase change in simulation 46 occurs over a 0.2 m interval between 751.0 and 751.2 m simulated depth, depending on the conductive fracture. This difference in phase partitioning is caused by fluid pressure variability, which in these simulations is solely a function of fracture permeability.

The ensemble e-type results for total CO_2 saturation at 10 years are presented in Figures 8c and 8f. These results show that CO_2 flow within the fracture network converges on a single path, while significant CO_2

saturation levels accumulate within less conductive fractures. This behavior is consistent with numerous studies that show flow path convergence in fracture-controlled, multiphase systems (Carneiro, 2009; Fairley et al., 2004; Glass et al., 2003; LaViolette et al., 2003; Wood et al., 2004; Zhou et al., 2006). In Pollyea and Fairley (2012a), the authors suggest that relative permeability effects may favor flow path convergence in strongly heterogeneous, multiphase fluid systems. In particular, these authors suggest a feedback mechanism in which resistance to flow along a given flow path decreases as CO_2 saturation increases, thus increasing CO_2 relative permeability and allowing further saturation gains along the flow path. In the context of CO_2 sequestration in basalt reservoirs, the nature of CO_2 flow paths to converge suggests that physical trapping may be significantly enhanced as carbonate minerals precipitate in the primary flow path.

In addition to flow path convergence, mean CO_2 saturation levels remain higher at locations within the fracture network where a single flow path branches and where conductive fractures terminate into the basalt matrix. This behavior is consistent with the early time results, and suggests that relative permeability effects encourage CO_2 accumulation at fracture intersections because CO_2 saturation levels are lower in the diverging fractures, thus inhibiting mobility through the intersection. Although this relative permeability effect at fracture intersections has not been shown experimentally, Glass et al. (2003) found that water tends to accumulate at fracture intersections during imbibition of an unsaturated fracture network. However, these authors proposed that water must overcome capillary barrier effects at a fracture intersection before advancing.

The corresponding standard deviation of total CO_2 saturation is also consistent with early time results in that maximum variability occurs in relatively straight flow paths (Figure 8f). This result arises because unsaturated flow in fracture networks is dependent on the properties of the entire path (Doughty, 2000). For each simulation in the Monte Carlo model, CO_2 follows the same fracture; however, the CO_2 saturation at any point is dependent on the permeability distribution along the entire fracture, including the permeability ahead of the advancing CO_2. This effect was shown by Kwicklis and Healy (1993), which used numerical methods to show that fluid flux varies spatially within a fracture network with variable aperture, even under saturated steady flow. For multiphase fluid systems, path-dependent flow is likely to be even more pronounced as relative permeability and capillary pressure effects introduce strongly nonlinear feedbacks within the fracture network.

In order to evaluate the effects of fracture permeability uncertainty on phase partitioning, individual e-type results for supercritical and gas phase CO_2 are presented in Figure 10. At simulated depths less than ∼750.8 m, the mean and standard deviation of supercritical phase CO_2 saturation are nil, which indicates that all CO_2 above 750.8 m is in the gas phase (Figures 10a and 10c). Similarly, for simulated depths greater than ∼752.4 m, the mean and standard deviation of gas phase CO_2 saturation are zero indicating that all free CO_2 below this depth is in the supercritical phase (Figures 10b and 10d). Consequently, the model scenario comprises a 1.6 m overlap in which phase partitioning is governed solely by the spatial distribution of fracture permeability. In this model scenario, temperature variations are orders of magnitude lower than pressure variations, and, as a result, the window of permeability-controlled phase partitioning is governed primarily by fluid pressure.

E-type results for fluid pressure after 10 years of simulation are shown in Figures 9c and 9f. The mean fluid pressure distribution is consistent with the 1 and 5 year results, except that the fluid pressure discontinuity is less pronounced at the horizontal position ∼2 m from the origin and 752.6 m depth. Similarly, the standard deviation of fluid pressure at this location is substantially lower due to pressure redistribution along the continuous flow path that develops through the fracture network. This flow path is demarcated by a near-vertical zone of pressure variability that is attributable to fracture permeability variability (Figure 9f). The effects of uncertainty in permeability within the conductive fracture are presented with greater detail in Figure 11. Within the conductive fracture, the effects of permeability uncertainty are
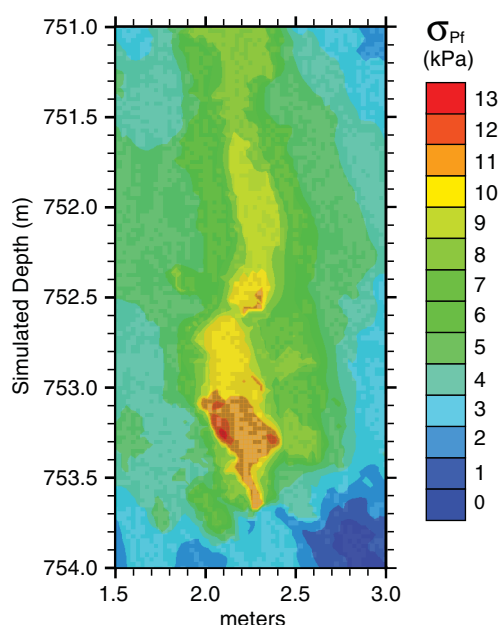

Figure 11. Detail subsection of Figure 9f with rescaled contour interval illustrating standard deviation of fluid pressure for the Monte Carlo model (N=50) after 10 years of simulation.

most pronounced between 753.0 and 753.5 m depth, where CO_2 is supercritical and fracture connectivity is restricted to a single grid cell. Within the overlapping phase-change interval (750.8–752.4 m), fluid pressure variability is comparatively lower ($\sim$10 kPa). The combined e-type estimates for fluid pressure, gas-phase CO_2, and supercritical phase CO_2 suggest that as buoyant supercritical CO_2 approaches the critical point, phase partitioning is highly sensitive to small changes in fluid pressure. These effects are complicated by volumetric expansion locally increasing fluid pressure, as well as the development of the three-phase zone that locally alters CO_2 mobility due to highly nonlinear, three-phase relative permeability and capillary pressure effects (Pruess, 2005). Since fluid pressure variability in the Monte Carlo model is solely a function of permeability distribution, these results suggest that CO_2 phase partitioning is strongly controlled by the fracture permeability distribution, which for this model occurs within a 1.6 m depth interval (thickness).

5. Conclusions

Successful field experiments in Washington State, USA, and Iceland yield compelling evidence that basalt reservoirs may be attractive targets for carbon capture and sequestration (Matter et al., 2016; McGrail et al., 2017). Nevertheless, industrial-scale implementation of this technology is hampered by still incomplete knowledge of multiphase flow characteristics in highly heterogeneous basalt fracture networks. This study is designed to gain insights into the behavior of CO_2 within the fracture network of an outcrop-scale flood basalt entablature when (1) the spatial distribution of fracture permeability is a priori unknown and (2) buoyant CO_2 undergoes phase change from supercritical fluid to subcritical liquid or gas. The primary results of this study are summarized below.

1. In early time ($\sim$1 year), CO_2 flow paths and fluid pressure are controlled primarily by fracture network geometry, while variability in CO_2 saturation is governed by interactions between fracture permeability and network geometry.
2. After 5 years of simulation, the ensemble (e-type) CO_2 saturation results show that CO_2 accumulates at fracture intersections, which suggests that mineralization may focus at these locations.
3. Ensemble calculations for subcritical and supercritical CO_2 after 10 years of simulation show that variations in fracture permeability result in a $\sim$1.6 m depth interval within which phase change occurs. This suggests that flood basalt entablature zones may exhibit favorable physical trapping characteristics for isolating CO_2 over time scales required for widespread mineralization.
4. For the model scenario, CO_2 flow tends to converge on a single flow path. This is consistent with previous investigations documenting similar behavior as water infiltrates an unsaturated fracture network (Fairley et al., 2004; Glass et al., 2003; LaViolette et al., 2003). In the context of CCS in flood basalt, the combination of CO_2 accumulation at fracture intersections and flow path convergence suggests that physical trapping within the low-permeability entablature zone may be significantly enhanced as carbonate minerals precipitate at fracture intersections and decrease overall fracture network connectivity.

In conclusion, these results suggest a theoretical possibility that the basalt-CO_2-water system may be self-sealing; however, significantly more research is needed to assess the likelihood of such an outcome in real world settings. Specifically, additional research is needed to more fully understand the nature of reactive permeability alteration, stress-dependent reservoir properties, and multiphase fluid properties in basalt fracture networks, and to incorporate these processes into reactive transport simulation codes.

Notation

α_{gl}	Capillary strength parameter for gas-liquid interface.
α_{la}	Capillary strength parameter for liquid-aqueous interface.
ϕ_f	Fracture porosity.
ϕ_m	Matrix porosity.
ω	Weighting function.
ρ_a	Aqueous phase density, kg m^{-3}.
ρ_r	Rock density, kg m^{-3}.
b	Fracture aperture, m.
c_p	Rock-grain specific heat capacity, J kg^{-1} °C^{-1}.
i	Summation index.

g	Acceleration due to gravity, m s^{-2}.
k_{eff}	Effective permeability, m^2.
k_f	Fracture permeability, m^2.
k_m	Matrix permeability, m^2.
k_{rg}	Relative permeability of gas or supercritical phase.
k_{ra}	Relative permeability of aqueous phase.
k_{rl}	Relative permeability of nonwetting liquid phase.
κ_T	Thermal conductivity, W m^{-1} °C^{-1}.
m	Van Genuchten (1980) phase interference parameter.
n	$n=1/(1-m)$.
$P_{c,ga}$	Capillary pressure across gas-aqueous interface, Pa.
$P_{c,gl}$	Capillary pressure across gas-liquid interface, Pa.
$P_{c,la}$	Capillary pressure across liquid-aqueous interface, Pa.
P_f	Fluid pressure, Pa.
S_a	Aqueous phase saturation.
$\overline{S}_a$	Effective wetting phase saturation.
S_g	Nonwetting gas or supercritical phase saturation.
$\overline{S}_g$	Effective gas or supercritical phase saturation.
S_l	Nonwetting phase liquid saturation.
$\overline{S}_l$	Effective nonwetting phase liquid saturation.
σ	Standard deviation, units of corresponding mean.
$T_\circ$	Initial temperature, °C.
TDS	Total dissolved solids, mg L^{-1}.

References

Adeoye, J. T., Menefee, A. H., Xiong, W., Wells, R. K., Skemer, P., Giammar, D. E., & Ellis, B. R. (2017). Effect of transport limitations and fluid properties on reaction products in fractures of unaltered and serpentinized basalt exposed to high P CO$_2$ fluids. *International Journal of Greenhouse Gas Control*, *63*, 310–320.

Bachu, S. (2008). CO$_2$ storage in geological media: Role, means, status and barriers to deployment. *Progress in Energy and Combustion Science*, *34*, 254–273.

Bacon, D. H., Ramanathan, R., Schaef, H. T., & McGrail, B. P. (2014). Simulating geologic co-sequestration of carbon dioxide and hydrogen sulfide in a basalt formation. *International Journal of Greenhouse Gas Control*, *21*, 165–176. https://doi.org/10.1016/j.ijggc.2013.12.012

Benson, S. M., & Cole, D. R. (2008). CO$_2$ sequestration in deep sedimentary formations. *Elements*, *4*, 325–331. https://doi.org/10.2113/gselements.4.5.325

Bertels, S. P., DiCarlo, D. A., & Blunt, M. J. (2001). Measurement of aperture distribution, capillary pressure, relative permeability, and in situ saturation in a rock fracture using computed tomography scanning. *Water Resources Research*, *37*, 649–662.

Camp, V. E. (1995). Mid-Miocene propagation of the Yellowstone mantle plume head beneath the Columbia River basalt source region. *Geology*, *23*(5), 435–438.

Carneiro, J. F. (2009). Numerical simulations on the influence of matrix diffusion to carbon sequestration in double porosity fissured aquifers. *International Journal of Greenhouse Gas Control*, *3*(4), 431–443.

Deutsch, C. V., & Journel, A. G. (1998). *GSLIB: Geostatistical software library and user's guide* (2nd ed.). New York, NY: Oxford University Press.

Doughty, C. (2000). Numerical model of water flow in a fractured basalt vadose zone: Box Canyon site, Idaho. *Water Resources Research*, *36*, 3521–3534.

Fairley, J. (2016). *Models and modeling: An introduction for earth and environmental scientists*. Hoboken, NJ: John Wiley & Sons.

Fairley, J., Podgorney, R., & Wood, T. (2004). Unsaturated flow through a small fracture–matrix network. *Vadose Zone Journal*, *3*(1), 101–108.

Ge, S. (1997). A governing equation for fluid flow in rough fractures. *Water Resources Research*, *33*, 53–61. https://doi.org/10.1029/96WR02588

Gislason, S. R., Wolff-Boenisch, D., Stefansson, A., Oelkers, E. H., Gunnlaugsson, E., Sigurdardottir, H., . . . Fridriksson, T. (2010). Mineral sequestration of carbon dioxide in basalt: A pre-injection overview of the CarbFix project. *International Journal of Greenhouse Gas Control*, *4*(3), 537–545. https://doi.org/10.1016/j.ijggc.2009.11.013

Glass, R. J., Nicholl, M. J., Rajaram, H., & Wood, T. R. (2003). Unsaturated flow through fracture networks: Evolution of liquid phase structure, dynamics, and the critical importance of fracture intersections. *Water Resources Research*, *39*(12), 1352. https://doi.org/10.1029/2003WR002015

Goldberg, D. S., Kent, D. V., & Olsen, P. E. (2010). Potential on-shore and offshore reservoirs for CO$_2$ sequestration in Central Atlantic magmatic province basalts. *Proceedings of the National Academy of Sciences of the United States of America*, *107*, 1327–1332. https://doi.org/10.1073/pnas.0913721107

Goldberg, D. S., Takahashi, T., & Slagle, A. L. (2008). Carbon dioxide sequestration in deep-sea basalt. *Proceedings of the National Academy of Sciences of the United States of America*, *105*, 9920–9925. https://doi.org/10.1073/pnas.0804397105

Gran, M., Zahasky, C., Garing, C., Pollyea, R., & Benson, S. (2017). Experimental study of relative permeability and saturation variations in a fractured basalt core. Paper presented at International Conference on Porous Media and Annual Meeting (InterPore), Rotterdam, The Netherlands.

Gysi, A. P., & Stefánsson, A. (2011). CO$_2$-water-basalt interaction. numerical simulation of low temperature CO$_2$ sequestration into basalts. *Geochimica et Cosmochimica Acta*, *75*(17), 4728–4751. https://doi.org/10.1016/j.gca.2011.05.037

Hooper, P., Binger, G., & Lees, K. (2002). Ages of the Steens and Columbia River flood basalts and their relationship to extension-related calc-alkalic volcanism in eastern Oregon. *Geological Society of America Bulletin*, *114*(1), 43–50.

Jayaraman, K. (2007). India's carbon dioxide trap. *Nature*, *445*, 350.

Jayne, R. S., & Pollyea, R. M. (2016). Constraining the effects of permeability uncertainty for geologic CO_2 sequestration in a basalt reservoir. Abstract CG41C-1110 presented at 2016 Annual Meeting of the American Geophysical Union, San Francisco, CA.

Jung, Y., Pau, G. S. H., Finsterle, S., & Pollyea, R. M. (2016). TOUGH3: A new efficient version of the TOUGH suite of multiphase flow and transport simulators. *Computers & Geosciences*, *108*, 2–7. https://doi.org/10.1016/j.cageo.2016.09.009

Kwicklis, E. M., & Healy, R. W. (1993). Numerical investigation of steady liquid water flow in a variably saturated fracture network. *Water Resources Research*, *29*, 4091–4102.

Lamur, A., Kendrick, J., Eggertsson, G., Wall, R., Ashworth, J., & Lavallée, Y. (2017). The permeability of fractured rocks in pressurised volcanic and geothermal systems. *Scientific Reports*, *7*, 6173. https://doi.org/10.1038/s41598-017-05460-4

LaViolette, R. A., Glass, R., Wood, T. R., McJunkin, T., Noah, R. K., Podgorney, R. K., . . . Stoner, D. L. (2003). Convergent flow observed in a laboratory-scale unsaturated fracture system. *Geophysical Research Letters*, *30*(2), 1083. https://doi.org/10.1029/2002GL015775

Lindberg, J. W. (1989). A numerical study of cooling joint width and secondary mineral infilling in four Grande ronde basalt flows of the central Columbia plateau, Washington. *Geological Society of America Special Papers*, *239*, 169–186.

Long, P. E., & Wood, B. J. (1986). Structures, textures, and cooling histories of Columbia River basalt flows. *Geological Society of America Bulletin*, *97*(9), 1144–1155.

Luhmann, A. J., Tutolo, B. M., Bagley, B. C., Mildner, D. F., Seyfried, W. E., & Saar, M. O. (2017a). Permeability, porosity, and mineral surface area changes in basalt cores induced by reactive transport of CO_2-rich brine. *Water Resources Research*, *53*, 1908–1927. https://doi.org/10.1002/2016WR019216

Luhmann, A. J., Tutolo, B. M., Tan, C., Moskowitz, B. M., Saar, M. O., & Seyfried, W. E. (2017b). Whole rock basalt alteration from CO_2-rich brine during flow-through experiments at 150°C and 150 bar. *Chemical Geology*, *453*, 92–110.

Mangan, M. T., Wright, T. L., Swanson, D. A., & Byerly, G. R. (1986). Regional correlation of Grande ronde basalt flows, Columbia river basalt group, Washington, Oregon, and Idaho. *Geological Society of America Bulletin*, *97*(11), 1300–1318. https://doi.org/10.1130/0016-7606(1986)97

Matter, J. M., & Kelemen, P. B. (2009). Permanent storage of carbon dioxide in geological reservoirs by mineral carbonation. *Nature Geoscience*, *2*, 837–841. https://doi.org/10.1038/NGEO683

Matter, J. M., Stute, M., Snæbjörnsdottir, S. Ó., Oelkers, E. H., Gislason, S. R., Aradottir, E. S., . . . Broecker, W. S. (2016). Rapid carbon mineralization for permanent disposal of anthropogenic carbon dioxide emissions. *Science*, *352*(6291), 1312–1314. https://doi.org/10.1126/science.aad8132

McGrail, B., Sullivan, E., Spane, F., Bacon, D., Hund, G., Thorne, P., . . . Colwell, F. (2009). Topical report—Preliminary hydrogeologic characterization results from the Wallula basalt pilot study (Tech. Rep. PNWD-4129). Richland, WA: Pacific Northwest National Laboratory.

McGrail, B. P., Schaef, H. T., Ho, A. M., Chien, Y.-J., & Dooley, J. J. (2006). Potential for carbon dioxide sequestration in flood basalts. *Journal of Geophysical Research*, *111*, B12201. https://doi.org/10.1029/2005JB004169

McGrail, B. P., Schaef, H. T., Spane, F. A., Cliff, J. B., Qafoku, O., Horner, J. A., . . . Sullivan, C. E. (2017). Field validation of supercritical CO_2 reactivity with basalts. *Environmental Science & Technology Letters*, *4*, 6–10. https://doi.org/10.1021/acs.estlett.6b00387

McGrail, B. P., Spane, F. A., Amonette, J. E., Thompson, C., & Brown, C. F. (2014). Injection and monitoring at the Wallula basalt pilot project. *Energy Procedia*, *63*, 2939–2948. https://doi.org/10.1016/j.egypro.2014.11.316

Nara, Y., Meredith, P. G., Yoneda, T., & Kaneko, K. (2011). Influence of macro-fractures and micro-fractures on permeability and elastic wave velocities in basalt at elevated pressure. *Tectonophysics*, *503*(1), 52–59. https://doi.org/10.1016/j.tecto.2010.09.027

Pacala, S., & Socolow, R. (2004). Stabilization wedges: Solving the climate problem for the next 50 years with current technologies. *Science*, *305*, 968–972. https://doi.org/10.1126/science.1100103

Parker, J., Lenhard, R., & Kuppusamy, T. (1987). A parametric model for constitutive properties governing multiphase flow in porous media. *Water Resources Research*, *23*, 618–624.

Pini, R., & Benson, S. M. (2013). Simultaneous determination of capillary pressure and relative permeability curves from core-flooding experiments with various fluid pairs. *Water Resources Research*, *49*, 3516–3530. https://doi.org/10.1002/wrcr.20274

Pollyea, R. (2016). Influence of relative permeability on injection pressure and plume configuration during CO_2 injections in a mafic reservoir. *International Journal of Greenhouse Gas Control*, *46*, 7–17. https://doi.org/10.1016/j.ijggc.2015.12.025

Pollyea, R. M., & Fairley, J. P. (2011). Estimating surface roughness of terrestrial laser scan data using orthogonal distance regression. *Geology*, *39*(7), 623–626. https://doi.org/10.1130/G32078.1

Pollyea, R. M., & Fairley, J. P. (2012a). Implications of spatial reservoir uncertainty for CO_2 sequestration in the east Snake River Plain, Idaho (USA). *Hydrogeology Journal*, *20*, 689–699. https://doi.org/10.1007/s10040-012-0847-1

Pollyea, R. M., & Fairley, J. P. (2012b). Experimental evaluation of terrestrial lidar-based surface roughness estimates. *Geosphere*, *8*(1), 1–7. https://doi.org/10.1130/GES00733.01

Pollyea, R. M., Fairley, J. P., Podgorney, R. K., & McLing, T. L. (2014). Physical constraints on geologic CO_2 sequestration in low-volume basalt formations. *Geological Society of America Bulletin*, *126*(3/4), 344–351. https://doi.org/10.1130/B30874.1

Pollyea, R. M., & Rimstidt, J. D. (2017). Rate equations for modeling carbon dioxide sequestration in basalt. *Applied Geochemistry*, *81*, 53–62. https://doi.org/10.1016/j.apgeochem.2017.03.020

Pruess, K. (2005). Numerical simulations show potential for strong nonisothermal effects during fluid leakage from a geologic disposal reservoir for CO_2. In *Dynamics of fluids and transport in fractured rock* (pp. 81–89). Washington, DC: American Geophysical Union.

Pruess, K. (2011). ECO2M: A TOUGH2 fluid property module for mixtures of water, NaCl, and CO_2, including super-and sub-critical conditions, and phase change between liquid and gaseous CO_2 (Tech. Rep. LBNL-4590E). Berkeley, CA: Lawrence Berkeley National Laboratory.

Ramos, F. C., Wolff, J. A., & Tollstrup, D. L. (2005). Sr isotope disequilibrium in Columbia River flood basalts: Evidence for rapid shallow-level open-system processes. *Geology*, *33*(6), 457–460. https://doi.org/10.1130/G21512.1

Reidel, S. (2015). The Columbia River Basalt Group: A flood basalt province in the Pacific Northwest, USA. *Geoscience Canada*, *42*, 151–168. https://doi.org/10.12789/geocanj.2014.41.061

Reidel, S. P., Camp, V. E., Tolan, T. L., & Martin, B. S. (2013). The Columbia River flood basalt province: Stratigraphy, areal extent, volume, and physical volcanology. *Geological Society of America Special Paper*, *497*, 1–43. https://doi.org/10.1130/2013.2497(01)

Rubin, Y. (2003). *Applied stochastic hydrogeology*. New York, NY: Oxford University Press.

Schaef, H., McGrail, B., & Owen, A. (2011). Basalt reactivity variability with reservoir depth in supercritical CO_2 and aqueous phases. *Energy Procedia*, *4*, 4977–4984. https://doi.org/10.1016/j.egypro.2011.02.468

Schaef, H., McGrail, B., Owen, A., & Arey, B. (2013). Mineralization of basalts in the CO_2-H_2O-H_2S system. *International Journal of Greenhouse Gas Control*, *16*, 187–196. https://doi.org/10.1016/j.ijggc.2013.03.020

Sigfusson, B., Gislason, S. R., Matter, J. M., Stute, M., Gunnlaugsson, E., Gunnarsson, I., . . . Oelkers, E. H. (2015). Solving the carbon-dioxide buoyancy challenge: The design and field testing of a dissolved CO_2 injection system. *International Journal of Greenhouse Gas Control*, *37*, 213–219. https://doi.org/10.1016/j.ijggc.2015.02.022

SIO. (2017). *The keeling curve, full record*. San Diego, Ca: Author. Retrieved from https://scripps.ucsd.edu/programs/keelingcurve/

Stone, H. (1970). Probability model for estimating three-phase relative permeability. *Journal of Petroleum Technology*, *22*(02), 214–218.

Tolan, T. L., Reidel, S. P., Beeson, M. H., Anderson, J. L., Fecht, K. R., & Swanson, D. A. (1989). Revisions to the estimates of the areal extent and volume of the Columbia River Basalt Group. *Geological Society of America Special Papers*, *239*, 1–20. https://doi.org/10.1130/SPE239-p1

Van Genuchten, M. (1980). A closed-form equation for predicting the hydraulic conductivity of unsaturated soils, *Soil. Science Society of America*, *44*, 892–898.

Vye-Brown, C., Self, S., & Barry, T. (2013). Architecture and emplacement of flood basalt flow fields: Case studies from the Columbia River Basalt Group, NW USA. *Bulletin of Volcanology*, *75*(3), 697. https://doi.org/10.1007/s00445-013-0697-2

Walker, R. J., Holdsworth, R. E., Armitage, P. J., & Faulkner, D. R. (2013a). Fault zone permeability structure evolution in basalts. *Geology*, *41*(1), 59–62. https://doi.org/10.1130/G33508.1

Walker, R. J., Holdsworth, R., Imber, J., Faulkner, D., & Armitage, P. (2013b). Fault zone architecture and fluid flow in interlayered basaltic volcaniclastic-crystalline sequences. *Journal of Structural Geology*, *51*, 92–104. https://doi.org/10.1016/j.jsg.2013.03.004

Witherspoon, P., Wang, J., Iwai, K., & Gale, J. (1980). Validity of cubic law for fluid flow in a deformable rock fracture. *Water Resources Research*, *16*, 1016–1024

Wood, T., Glass, R., McJunkin, T., Podgorney, R., Laviolette, R., Noah, K., . . . Baker, K. (2004). Unsaturated flow through a small fracture–matrix network. *Vadose Zone Journal*, *3*(1), 90–100.

Wood, W. W., & Fernandez, L. (1988). Volcanic rocks. In W. Back, J. Rosenshein, & P. Seaber (Eds.), *The geology of North America, Vol. O-2. Hydrogeology* (chap. 39, pp. 353–365). Boulder, CO: Geological Society of America.

Zakharova, N. V., Goldberg, D. S., Sullivan, E. C., Herron, M. M., & Grau, J. A. (2012). Petrophysical and geochemical properties of Columbia River flood basalt: Implications for carbon sequestration. *Geochemistry, Geophysics, Geosystems*, *13*, Q11001. https://doi.org/10.1029/2012GC004305

Zhou, Q., Salve, R., Liu, H.-H., Wang, J. S., & Hudson, D. (2006). Analysis of a mesoscale infiltration and water seepage test in unsaturated fractured rock: Spatial variabilities and discrete fracture patterns. *Journal of Contaminant Hydrology*, *87*(1), 96–122.